

Infrared $\text{Al}_{0.15}\text{InAsSb}$ Digital Alloy $n\text{Bn}$ Photodetectors

Renjie Wang , J. Andrew McArthur , Seth R. Bank , *Fellow, IEEE*, and Joe C. Campbell , *Fellow, IEEE*

Abstract—AllInAsSb photodetectors with high detectivity at 2 μm and 2.7 μm are reported. For 2- μm photodetection, figure-of-merit characteristics including specific detectivity, D^* , responsivity, dark current density, and differential-resistance area product of two photodetectors employing respectively $\text{Al}_{0.15}\text{InAsSb}$ and $\text{Al}_{0.3}\text{InAsSb}$ absorbers are compared and analyzed from 90 to 300 K. Peak D^* of 1.1×10^{12} Jones for 2- μm photodetection was obtained at -0.1 V bias and 180 K and 4.9×10^9 Jones for 2.7- μm photodetection at room temperature was obtained at -0.25 V bias. Close agreement was observed between dark current density and D^* for different mesa diameters, an important consideration for focal plane arrays. The bias for peak D^* , V_{peak} , was considerably reduced by using a proper doping concentration in the bottom contact layer. The measured V_{peak} , and the derived absorption coefficient and minority carrier diffusion length at different temperatures, provide improved understanding of the Al_xInAsSb material for $n\text{Bn}$ photodetectors.

Index Terms—III-V semiconductor, photodetectors, responsivity, specific detectivity.

I. INTRODUCTION

THE n -barrier- n ($n\text{Bn}$) photodetectors operate with low voltage and small depletion in the narrow bandgap absorber [1], [2]. With their advantages of low Shockley-Read-Hall (SRH) generation, low tunneling current, and high specific detectivity (D^*), high performance infrared detectors have been achieved [3]–[7]. They have become key detectors for imaging and sensing applications in the 2.0 μm to 5.0 μm spectral region. The $n\text{Bn}$ photodetectors have been fabricated from various III-V semiconductors, including InAs/InAsSb superlattices [3]–[5], InAs/GaSb superlattices [6], and InGaAsSb bulk alloy [7]. Recently, the $\text{Al}_x\text{In}_{1-x}\text{As}_y\text{Sb}_{1-y}$ (referred to as Al_xInAsSb) material system has been shown to be a promising material candidate because its valence band offset is near-zero for varying compositions ($x \approx 0$ to 0.8) [8]. The initial demonstration with this

material used an $\text{Al}_{0.3}\text{InAsSb}/\text{Al}_{0.7}\text{InAsSb}$ structure employing an $\text{Al}_{0.3}\text{InAsSb}$ absorber (the bandgap energy, $E_g = \sim 0.58$ eV) and an $\text{Al}_{0.7}\text{InAsSb}$ barrier ($E_g = \sim 1.16$ eV) [9]. The cut-off wavelength of $\text{Al}_{0.3}\text{InAsSb } n\text{Bn}$ has been determined to be ~ 2.1 μm at room temperature by measuring its wavelength-dependent quantum efficiency [10]. These photodetectors achieved a peak D^* of 1.7×10^{10} Jones under 2- μm illumination at room temperature. To achieve high D^* operation, it is desirable to maximize the responsivity, \mathfrak{R} , and minimize both the dark current density, J_d , and $1/(RA)$ where RA is the differential-resistance area product [1], [3], [6], [7]. The J_d and $1/(RA)$ in the SRH/diffusion-dominated regime can be dramatically reduced by operating at cryogenic temperatures [1], [3], [5], [7], [11]. However, the lower temperature may also lead to a smaller \mathfrak{R} due to a smaller absorption coefficient, α , of the absorber [12], [13] and a smaller minority carrier diffusion length, L_{diff} [13]. The temperature dependence of \mathfrak{R} and D^* of $\text{Al}_{0.3}\text{InAsSb } n\text{Bn}$ photodetectors was not investigated in the previous work. Also, using a lower bandgap absorber such as $\text{Al}_{0.15}\text{InAsSb}$ absorber ($E_g = \sim 0.42$ eV [14]), can provide higher room-temperature \mathfrak{R} for 2- μm photodetection, compensate the blueshift of absorption edge towards 2 μm at lowered temperature, and extend the cutoff to ~ 3 μm . The $\text{Al}_{0.15}\text{InAsSb } n\text{Bn}$ photodetectors operating with high specific detectivity in the 2–3 μm “eye-safe” wavelength range are promising for a variety of civilian, military, and scientific applications. These include detection and ranging (LIDAR) [15], [16], satellite and terrestrial imaging [17], earth observation [18], [19], and biological [17] and chemical [20] detection and process monitoring.

The parameters \mathfrak{R} , J_d , and $1/RA$ also depend on applied bias, which results in the bias dependence of D^* . The peak D^* of $n\text{Bn}$ photodetectors is generally obtained at low bias, V_{peak} , where D^* reaches the maximum value, D^*_{peak} [6], [10]. At a bias higher than V_{peak} the increase of \mathfrak{R} cannot compensate the increase of J_d and $1/RA$, whereas \mathfrak{R} decreases dramatically at a bias lower than V_{peak} [10]. Therefore, it is beneficial to reduce V_{peak} to minimize SRH generation and tunneling for higher D^*_{peak} as well as to achieve near-zero-bias operation. There have been few reports on the temperature dependence of V_{peak} . In this paper we show that the temperature dependence of V_{peak} changes depending on whether SRH/diffusion or tunneling mechanisms dominate J_d and $1/RA$ [10], [21]. This is important for understanding the optimum bias range for $n\text{Bn}$ operation and provides insight to observations that were not explained in our previous work [10].

In this work, $n\text{Bn}$ photodetectors employing $\text{Al}_{0.15}\text{InAsSb}$ digital alloy absorber are demonstrated with high D^* at 2- μm

Manuscript received November 24, 2021; revised February 1, 2022; accepted February 5, 2022. Date of publication February 9, 2022; date of current version June 16, 2022. This work was supported in part by the Army Research Office and DARPA under Grant W911NF-17-1-0065, in part by DARPA under Grant W909MY-12-D-0008, and in part by the National Science Foundation under Grant ECCS-1933836. (Corresponding author: Joe C. Campbell.)

Renjie Wang and Joe C. Campbell are with the Department of Electrical and Computer Engineering, University of Virginia, Charlottesville, VA 22904 USA (e-mail: qmq2bt@virginia.edu; jcc7s@virginia.edu).

J. Andrew McArthur and Seth R. Bank are with the Department of Electrical and Computer Engineering, The University of Texas, Austin, TX 78758 USA (e-mail: jandrewmcarthur@utexas.edu; sbank@ece.utexas.edu).

Color versions of one or more figures in this article are available at <https://doi.org/10.1109/JLT.2022.3149773>.

Digital Object Identifier 10.1109/JLT.2022.3149773

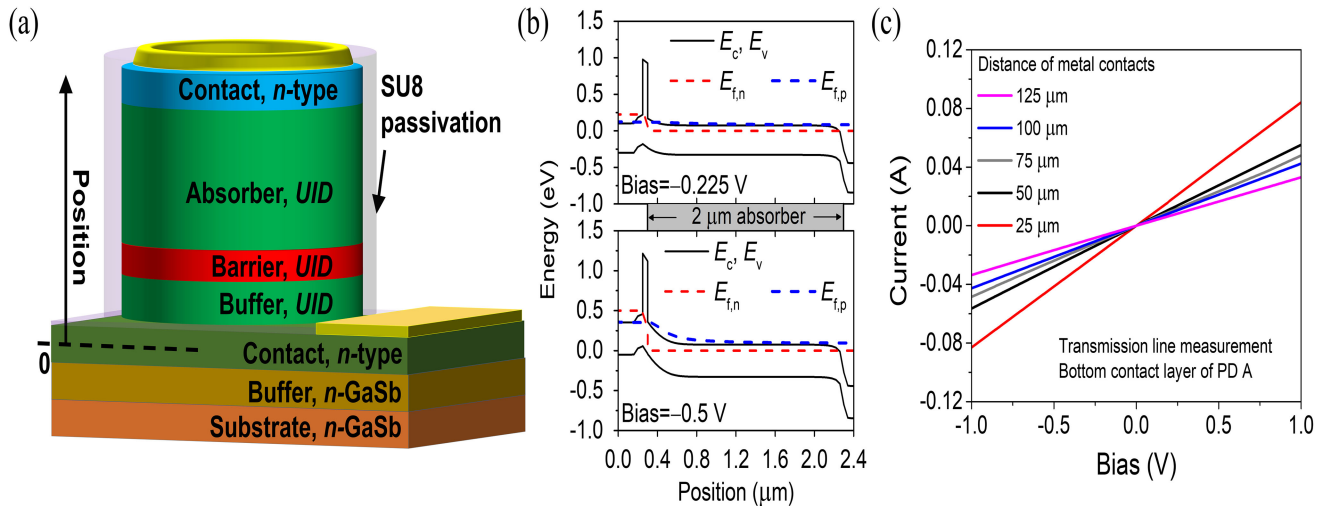


Fig. 1. (a) Schematic illustration of the PD A and PD B $\text{Al}_x\text{InAsSb}/\text{Al}_{0.7}\text{InAsSb}$ $n\text{Bn}$ photodetectors, (b) energy band diagram of PD A at -0.225 V and -0.5 V, and (c) TLM current-voltage results of PD A bottom contact with the doping concentration of $1 \times 10^{18} \text{ cm}^{-3}$.

and $2.7\text{-}\mu\text{m}$ wavelengths. For $2\text{-}\mu\text{m}$ photodetection, the D^*_{peak} of 1.1×10^{12} Jones was obtained at -0.1 V and 180 K and 2.5×10^{12} Jones was obtained at -0.15 V bias and 130 K. For $2.7\text{-}\mu\text{m}$ photodetection at room temperature, D^*_{peak} of 4.9×10^9 Jones was obtained at -0.25 V bias. For $2\text{-}\mu\text{m}$ photodetection, the figure-of-merit characteristics including D^* , \mathcal{R} , J_d and RA of two photodetectors employing respectively $\text{Al}_{0.15}\text{InAsSb}$ and $\text{Al}_{0.3}\text{InAsSb}$ absorbers are compared and analyzed in the temperature range $T = 90\text{--}300$ K. V_{peak} was considerably reduced by using a proper doping concentration in contact layer. The V_{peak} , α , and L_{diff} at different temperatures were studied to gain more understanding of the Al_xInAsSb material for $n\text{Bn}$ photodetectors to help improve device performance. This work also compares the diameter dependence of I_d and D^* , which is an important consideration for focal plane arrays.

II. EPITAXIAL STRUCTURE AND DEVICE FABRICATION

The $n\text{Bn}$ photodetectors based on the $\text{Al}_{0.15}\text{InAsSb}$ absorber and the $\text{Al}_{0.3}\text{InAsSb}$ absorber are respectively represented by PD A and PD B in the following text. Fig. 1(a) illustrate their layer structure. The $n\text{Bn}$ structures were grown on n -type GaSb substrates as digital alloys lattice matched to GaSb by molecular beam epitaxy [14]. Corresponding to each layer shown in Fig. 1(a), their material, layer thickness, and doping concentration are summarized in Table I. They were grown with some common features, such as the $2\text{-}\mu\text{m}$ absorber thickness and the $\text{Al}_{0.7}\text{InAsSb}$ barrier.

Both PD A and PD B were fabricated into circular mesa structures using standard photolithography techniques, acid wet etching, and SU-8 surface passivation. A citric acid solution was used for wet etching, and it consisted of 10 g citric acid, 60 ml DI water, 6 ml H_3PO_4 , and 3 ml H_2O_2 . We note that the etching rate of $\text{Al}_{0.15}\text{InAsSb}$ is slower than that of $\text{Al}_{0.3}\text{InAsSb}$ when the same citric acid solution is used. The circular mesas were 60, 80, 100, 150, 200, 250 and 350 μm in diameter. Titanium/gold

TABLE I
MATERIAL, LAYER THICKNESS, AND DOPING CONCENTRATION OF PD A AND PD B DEVICES

Layer	PD A			PD B		
	Material	Thickness	Doping	Material	Thickness	Doping
Top contact	$\text{Al}_{0.15}\text{InAsSb}$	0.1 μm	$5 \times 10^{18,a}$	$\text{Al}_{0.3}\text{InAsSb}$	0.1 μm	$5 \times 10^{18,a}$
Absorber	$\text{Al}_{0.15}\text{InAsSb}$	2 μm	UID ^b	$\text{Al}_{0.3}\text{InAsSb}$	2 μm	UID ^b
Barrier	$\text{Al}_{0.7}\text{InAsSb}$	0.05 μm	UID ^b	$\text{Al}_{0.7}\text{InAsSb}$	0.05 μm	UID ^b
Buffer	$\text{Al}_{0.15}\text{InAsSb}$	0.05 μm	UID ^b	$\text{Al}_{0.3}\text{InAsSb}$	0.15 μm	UID ^b
Bottom contact	$\text{Al}_{0.15}\text{InAsSb}$	0.4 μm	$1 \times 10^{18,a}$	$\text{Al}_{0.3}\text{InAsSb}$	0.4 μm	$5 \times 10^{18,a}$

^aDoping concentration (cm^{-3}).

^bAbbreviation for *unintentionally doped*.

contacts were deposited onto the top and bottom contact layers of the $n\text{Bn}$ structures.

Compared to PD B, a lower doping concentration was used for the PD A bottom contact layer. This can reduce the flattened-valence-band voltage, V_{fvb} , which flattens the valence band (VB) barrier between the bottom contact layer and the *unintentionally doped* (UID) absorber. Their energy band diagram and the effects of bottom-contact doping concentration on V_{fvb} , D^*_{peak} and V_{peak} of PD A were studied based on the simulations of Lumerical device suite (ANSYS) including Finite Difference Time Domain solver [22] for optical generation and CHARGE solver [23] for charge transport. Multi-coefficient models are used to describe the properties and processes of semiconductor layers [24]. The Al_xInAsSb material parameters used for the simulations of the energy band diagram are based on an approximate formula in which its material parameters are assumed to be a linear combination of InAs, AlSb, AlAs and InSb material parameters [25]–[27]. Fig. 1(b) shows the PD A energy band diagram at 300 K with $V_{\text{fvb}} = -0.225$ for the doping concentration of $1 \times 10^{18} \text{ cm}^{-3}$. The generated holes can

transport to the bottom contact layer at both -0.225 V and -0.5 V bias (bias $\geq V_{\text{fvb}}$), whereas the holes are impeded by the VB barrier for bias below V_{fvb} . Its D^*_{peak} is obtained at the bias of $V_{\text{peak}} = -0.25$ V for the doping concentration of 1×10^{18} cm⁻³. When the PD A bottom-contact doping concentration is increased to 5×10^{18} cm⁻³, the simulation shows that its V_{fvb} increases to -0.475 V and its V_{peak} increases to -0.5 V. The simulations shows that D^*_{peak} is higher for the lower doping concentration which leads to a lower V_{fvb} and thus a lower V_{peak} . The PD B bottom-contact doping concentration is 5×10^{18} cm⁻³, and the PD B simulation shows $V_{\text{fvb}} = -0.475$ V and $V_{\text{peak}} = -0.5$ V.

Transmission line measurements (TLM) were carried out for the PD A and PD B bottom contacts to measure their specific contact resistivity, ρ_c , and sheet resistivity, R_s . Shown in Fig. 1(c), the TLM results of PD A bottom contact show linear current-voltage (I - V) characteristics and their slopes depend on the distance between the metal contacts. The ρ_c and R_s of the PD A bottom contact were measured to be 2.0×10^{-4} $\Omega \cdot \text{cm}^2$ and 33.5 Ω , respectively. The ρ_c and R_s of PD B bottom contact with a higher doping concentration of 5×10^{18} cm⁻³ were measured to be 1.8×10^{-4} $\Omega \cdot \text{cm}^2$ and 31.7 Ω , respectively. This indicates that the decrease of doping concentration in PD A bottom contact layer does not degrade its contact properties.

III. DEVICE CHARACTERIZATION

Temperature-dependent current-voltage measurements were carried out in a liquid N₂-cooled cryogenic probe station (LakeShore Cryogenics) at $T = 80$ – 300 K with a temperature controller (LakeShore, 336), and a precision semiconductor parameter analyzer (Agilent, 4155C). These measurements were done in the dark and with 2 - μm illumination from a laser diode (Thorlabs, CLD1015). Capacitance-voltage (C - V) characteristics were also measured at $T = 80$ – 300 K with a calibrated LCR meter (HP 4275A). The current-voltage characteristics were also measured at room temperature with 2.7 - μm illumination from an erbium-doped ZrF₄ fiber laser (Thorlabs, LFL2700).

IV. RESULTS AND DISCUSSION

Fig. 2(a) shows current-voltage curves for a 350 - μm -diameter PD A in the dark at $T = 80$ – 300 K and the calculated J_d is shown at the right axis. To gain an understanding of the I_d sources, diameter-dependent current-voltage measurements were carried out for PD A at 300 K and 80 K and PD B at 300 K and 120 K. Fig. 2(b) summarizes the measured I_d of PD A (solid symbols) at -0.25 V, -0.5 V, -2 V, and -4 V and PD B (hollow symbols) at -0.5 V. The I_d of PD A increases quadratically with mesa diameter (D) and the PD A data points match well with fitting curves of $I_d = D^2 \times \text{Constant}$, which suggests that bulk mechanisms [28] dominate the I_d sources of PD A. Different from PD A, the measured I_d data points of PD B deviate from the curves of $I_d = D^2 \times \text{Constant}$ and the calculated J_d decreases with D , which suggests the surface defects assume a significant role for PD B [10]. A quantitative assessment on the bulk and surface components of J_d and RA of PD B can be found in our previous work [10]. At -0.5 V and 300 K, I_d of PD A

TABLE II
DARK CURRENT DENSITY AND 2 - μm RESPONSIVITY OF PD A AT -0.25 V AND PD B AT -0.5 V, RESISTANCE-AREA PRODUCT, AND PEAK SPECIFIC DETECTIVITY AND BIAS FOR 2 - μm PHOTODETECTION

T (K)	J_d (A/cm ²)		\Re (A/W)		R_0A (Ωcm^2)		Peak D^* (Jones), V_{peak} (V)	
	PD A	PD B	PD A	PD B	PD A	PD B	PD A	PD B
300	1.4×10^{-2}	1.8×10^{-3}	0.62	0.41	2.2×10^2	4.3×10^3	9.2×10^9 , -0.25	1.7×10^{10} , -0.5
180	1.7×10^{-7}	5.9×10^{-8}	0.16	0.09	8.4×10^7	1.0×10^9	1.1×10^{12} , -0.1	1.0×10^{12} , -0.25
120	5.5×10^{-9}	1.4×10^{-10}	0.10	0.01	2.7×10^8	7.4×10^9	2.4×10^{12} , -0.15	1.7×10^{12} , -0.35
90	4.6×10^{-9}	1.0×10^{-11}	0.09	0.01 ^a	3.0×10^8	7.9×10^9	2.2×10^{12} , -0.15	1.4×10^{12} , -0.35

^aThe value 0.01 A/W was obtained by rounding up the measured value.

is around one order of magnitude higher than that of PD B. The I_d difference between PD A and PD B and the difference between their diameter dependences are mainly attributed to the significant increase of dark current in PD A bulk region, because the same device fabrication process was used for PD A and PD B. For PD A, the percentage of its surface leakage current in the total dark current is small, compared to its large bulk dark current.

The $1/kT$ dependence of I_d and RA for a 350 - μm -diameter PD A at different bias is plotted in Fig. 2(c) and (d), respectively. The regime of $T = 190$ – 300 K is diffusion/SRH-dominated, and I_d and $1/RA$ follow an Arrhenius relation with T . I_d and $1/RA$ versus $1/kT$ suggest a band-to-band process at low biases and SRH-dominated process at higher biases, because SRH generation current increases with bias [10], [29]. Similar plots of J_d and RA versus $1/kT$ for PD B can be found in [10]. I_d and RA can be fit using the following relations [1], [2], [10]:

$$I_d \propto n_i^2 \propto T^3 \exp(-\Delta E/kT), \quad (1)$$

$$RA \propto T^{1/2}/n_i^2 \propto T^{-5/2} \exp(\Delta E/kT) \quad (2)$$

where n_i is the intrinsic concentration, ΔE is the activation energy, and k is the Boltzmann constant. ΔE determines the slopes of I_d and RA versus $1/kT$; ΔE of PD A is 0.42 eV at -0.1 V, and it decreases with reverse bias due to the increased contribution of SRH at higher bias. The regime of $T = 80$ – 120 K is tunneling-dominated [10]. For the 350 - μm -diameter devices, the calculated J_d of PD A at -0.25 V and PD B at -0.5 V, and R_0A of PD A and PD B are summarized in Table II. Taking the background-limited infrared photodetection (BLIP) condition to be $1/4$ of the photocurrent [1], [4], [10], unshielded measurements at -0.1 V bias revealed a BLIP temperature of ~ 186 K for PD A.

Fig. 3(a) and (b) show respectively current-voltage curves and \Re versus applied bias for a 350 - μm -diameter PD A measured under 2 - μm laser illumination of 1322.1 W/m² irradiance and at $T = 80$ – 300 K. Shown in Fig. 3(b), \Re increases with temperature. The temperature-dependent \Re of a 350 - μm -diameter PD A at -0.25 V and a PD B at -0.5 V are summarized in Table II.

Based on the measured I_d , RA , and \Re at different temperatures, D^* of 350 - μm -diameter PD A and PD B under 2 - μm

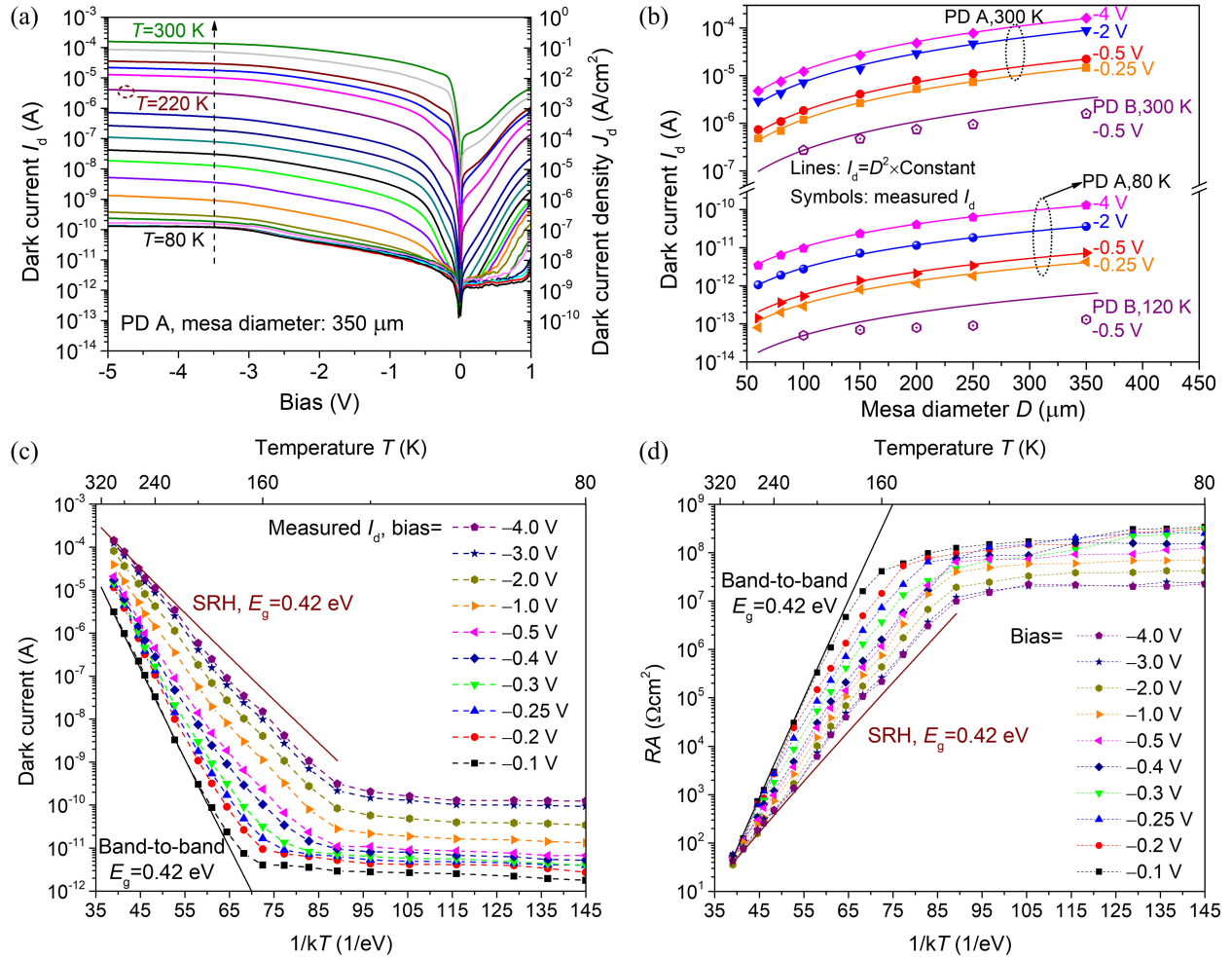


Fig. 2. (a) Current-voltage curves of a 350-μm-diameter PD A in the dark at $T = 80$ – 300 K. (b) I_d versus diameter, D , for PD A at 300 K and 80 K and PD B at 300 K and 120 K. The solid symbols represent I_d of PD A measured at -4 V, -2 V, -0.5 V, and -0.25 V, and the hollow symbols represent I_d of PD B measured at -0.5 V. The solid lines $I_d = D^2 \times \text{Constant}$ show the bulk-dominated I_d for PD A. Plots of the $1/kT$ dependence of (c) I_d and (d) RA for -0.1 V to -4.0 V bias applied to a 350-μm diameter PD A. The top axis shows the corresponding T . The solid lines show the slopes of ideal SRH and diffusion relations [1], [2] for $E_g = 0.42$ eV.

laser illumination of 1322.1 W/m² irradiance are calculated [3], [6], [7] and shown in Fig. 3(c) and (d), respectively. The temperature-dependent D^*_{peak} of a 350-μm-diameter PD A and PD B are summarized in Table II. The D^*_{peak} increases from $\sim 10^9$ Jones at 300 K to $\sim 10^{12}$ Jones at 180 K, which is primarily due to the decrease of both J_d and $1/RA$ with a factor of ~ 5 in the diffusion/SRH-dominated regime shown in the low-bias data points of Fig. 2(c) and (d). Relatively mild increases in D^*_{peak} are observed in the transitional regime at $T = 130$ – 180 K. The D^*_{peak} of PD A at 130 K was measured to be 2.5×10^{12} Jones at -0.15 V bias. The D^*_{peak} does not increase in the tunneling-dominated regime of $T \leq 120$ K where J_d and $1/RA$ do not depend on the temperature but the measured \mathcal{R} decreases with temperature.

Substantial progress on 2-μm photodetection has been achieved with other detector technologies, such as HgCdTe avalanche photodiodes (APD) [30] and InAs APDs [31]. Besides Al_{0.3}InAsSb digital alloy nBn photodetectors, Al_{0.3}InAsSb p - i - n APDs [32] and Al_{0.3}InAsSb separate absorption, charge, and

multiplication (SACM) APDs [16] have been developed for extended short-wavelength infrared photodetection. The 1550-nm responsivity of a 150-μm-diameter Al_{0.3}InAsSb p - i - n detector was reported to be 0.425 A/W, corresponding to a thermal noise equivalent power of 6.15×10^{-14} W/Hz^{1/2} [32]. Photodetection at 2 μm has also been reported for HgCdTe n - on - p detectors [33], InAs/GaSb/InAsSb/GaSb interband cascade detectors [34], and fluorographene photoconductive detectors [35]. Their specific detectivities and other figure-of-merit parameters are shown in Table III."

V_{peak} of PD A and PD B devices at 300 K were measured to be respectively -0.25 V and -0.5 V, which nearly equals the simulated V_{fvb} . The temperature dependences of V_{peak} are shown along the peak- D^* dashed lines of Figs. 3(c) and (d) as well as the summaries of V_{peak} in Table II. The temperature dependence of V_{peak} is greatly affected by the temperature dependence of J_d and $1/RA$ in different temperature regimes. In the diffusion/SRH-dominated regime ($T = 190$ – 300 K), J_d and $1/RA$ at a lower bias decreases faster than those at higher bias,

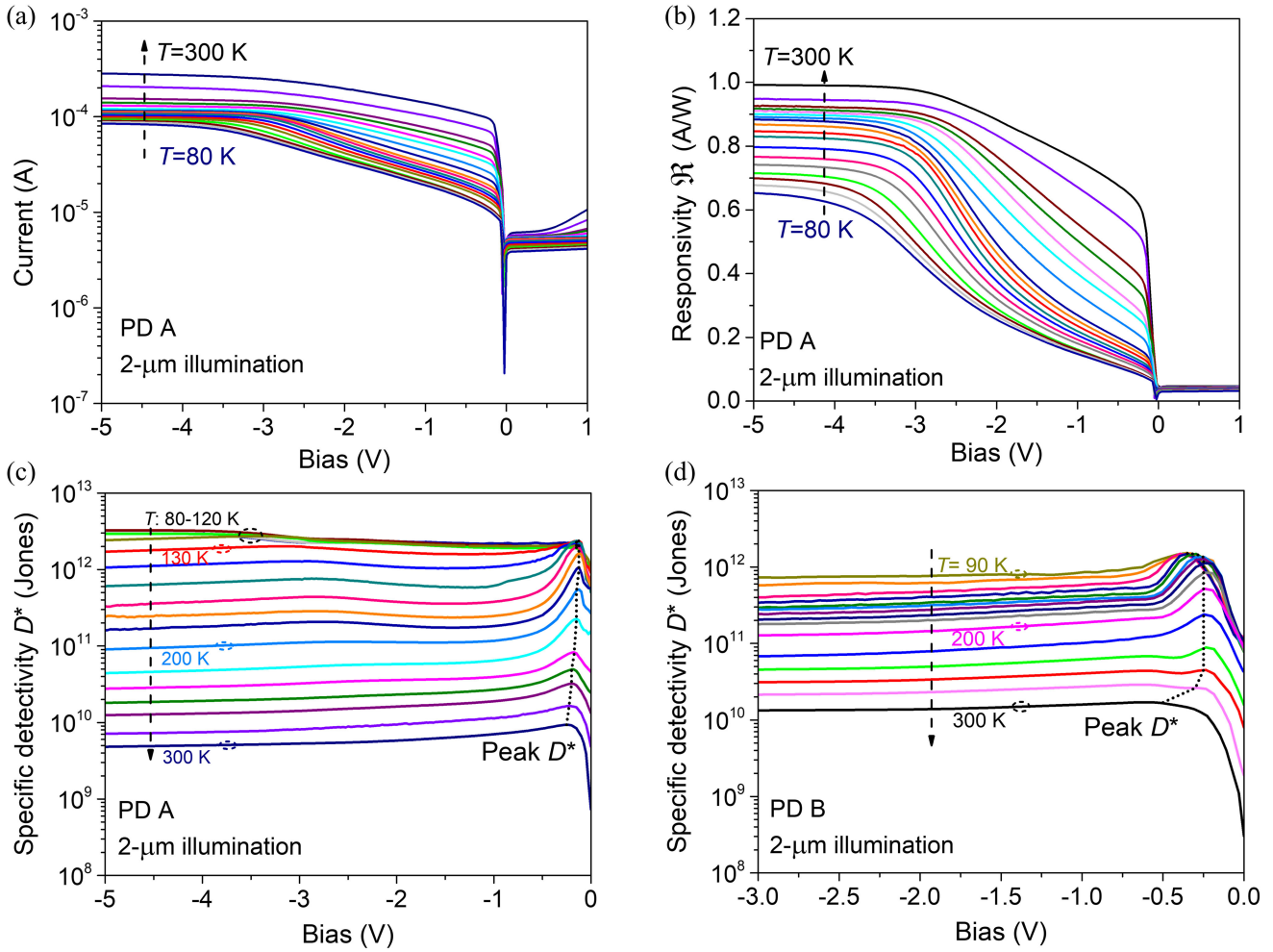


Fig. 3. (a) Current. (b) \mathcal{R} (linear scale). (c) D^* versus applied bias of a 350- μm -diameter PD A measured under 2- μm illumination and at $T = 80\text{--}300$ K. (d) D^* of a 350- μm -diameter PD B measured under 2- μm illumination and at $T = 90\text{--}300$ K.

TABLE III
REPORTS ON 2- μm SPECIFIC DETECTIVITY, DARK CURRENT DENSITY, RESPONSIVITY, AND RESISTANCE-AREA PRODUCT

Photodetector [Reference]	λ (μm)	T (K), Maximum D^* ($\times 10^9$ Jones), Bias (V)	T (K), J_d (A/cm^2), Bias (V)	T (K), \mathcal{R} (A/W)	T (K), R_0A (Ωcm^2),	Size (μm^2)
Hg _{0.53} Cd _{0.47} Te, <i>n-on-p</i> [33]	~2.0	246 K, 200, -; 193 K, 3000, -	-	-	246 K, ~800; 193 K, 8×10^4	254 \times 254
InAs/GaSb/InAsSb/GaSb, Interband cascade [34]	2.1	300 K, 7.5, -0.3	300 K, $\sim 4 \times 10^{-2}$, -0.3; 250 K, $\sim 2.5 \times 10^{-3}$, -0.3	300 K, -0.45; 250 K, -0.43	300 K, 7.84; 250 K, 237	200 \times 200
Broadband fluorographene, Photoconductive [35]	1.87	77 K, ~ 10 , 1 ^a	-	-	-	150 \times 50

^aDrain-source voltage.

because the derived ΔE decreases with the applied bias. As a result, in the diffusion/SRH-dominated regime, V_{peak} decreases with decreasing temperature, and it reaches the minimum at $T = 180\text{--}190$ K. In our previous work which used a bias step size of 0.1 V for current-voltage measurements, V_{peak} for PD B was measured to be -0.5 V at room temperature, however, its highest BLIP temperature of ~ 180 K was obtained at -0.3 V [10]. The temperature dependence of V_{peak} revealed in this work explains

the reasons these two bias values differ. In the transitional regime ($T = 130\text{--}180$ K), the increases in V_{peak} are relatively small, because J_d and $1/RA$ at higher bias decrease moderately faster than those at lower bias as shown in Fig. 2(c) and (d) for PD A as well as in our previous work for PD B [10].

The diameter dependence of D^* is primarily determined by the diameter dependence of J_d and $1/RA$. For PD A with mesa diameters of 100 to 350 μm , the variation of D^* is within $\pm 4\%$,

since the bulk mechanism dominates its J_d and $1/RA$. Different from PD A, the D^* of PD B increases with diameter, since its J_d and $1/RA$ decrease with mesa diameter. The D^*_{peak} of a 350- μm -diameter PD B was measured to be around 45% higher than that for a 100- μm diameter. For 350- μm -diameter devices at 300 K, the PD A D^*_{peak} is smaller than that of PD B. However, for $T = 130\text{--}300$ K, larger increases of D^*_{peak} were measured from PD A than that of PD B, as shown in Table II. D^*_{peak} of PD A is $\sim 10\%$ higher than that of PD B at 180 K and their difference increases to 41% at 120 K.

D^* is also greatly affected by the temperature dependence of \mathfrak{R} . The temperature-dependent \mathfrak{R} largely contributes to the result that the D^*_{peak} of PD A is higher at $T = 90\text{--}200$ K but lower at $T = 220\text{--}300$ K than those of PD B. Quantitative analyses of the bias-dependent \mathfrak{R} at different temperatures were conducted by using a theoretical model developed and used in the literatures [13], [27], [36]. In this model, the photoexcited carriers diffuse in the undepleted region and those in the depleted region are swept into the contact. The total photocurrent includes the contributions from the undepleted and depleted regions. This model gives analytical equations that can be expressed as $\mathfrak{R} = f(w)$ which is where q is the electronic charge, λ is the illumination wavelength, h is Planck's constant, c is the speed of light, r is the reflection coefficient, t is the top-contact thickness, L_{diff} is the minority carrier diffusion length, H is the thickness of absorption layer, w is the depletion width, and $b = (H-w)/L_{\text{diff}}$ [13], [27], [36].

The bias-dependent w was derived from C - V measurements by using the equations in Ref. [37]. C - V measurements were conducted at $T = 80\text{--}300$ K and the PD A results are shown in Fig. 4(a). The measured capacitance of PD A and PD B increases with temperature. This observation agrees with the report that the dielectric constant increases with temperature for compound semiconductors investigated at $T = 100\text{--}300$ K [38]. Shown in Fig. 4(a), the 2- μm thick absorber is fully depleted at -7 V bias, considering that the difference between the measured capacitance at -7 V and that at -6 V is less than 0.4%. The bias-dependent \mathfrak{R} was fit with the bias-dependent w by using $f(w)$ for each temperature. Fig. 4(b) and (c) show respectively the model fitting for PD A and PD B. Shown in the Fig. 4(d), the derived α and L_{diff} decrease with temperature, which results in the decrease of \mathfrak{R} with decreasing temperature. This also reveals the mechanisms of the decreasing D^* with decreasing temperature in the tunneling-dominated regime where the decrease of I_d and $1/RA$ are negligible.

The derived α considerably decreases with temperature, which agrees with the reported α of InGaAs investigated at $T = 5\text{--}301$ K [12]. The decrease in α at low temperature can be attributed to several temperature-dependent factors, including the blue-shift of absorption edge with increasing bandgap and changes in the density of states [13]. The cutoff wavelength of

$\text{Al}_{0.3}\text{InAsSb}$ at room temperature is around 2.1 μm [10]. The 2- μm α of $\text{Al}_{0.3}\text{InAsSb}$ decreases by $\sim 97\%$ as the temperature decreases from 300 to 90 K, which is mainly resulted from the blueshift of the absorption edge towards 2 μm . The α of $\text{Al}_{0.15}\text{InAsSb}$ is significantly higher than that of $\text{Al}_{0.3}\text{InAsSb}$ at $T = 90\text{--}300$ K due to the lower bandgap.

As shown in Fig. 4(d), the derived minority carrier diffusion length, L_{diff} , also decreases with temperature, which agrees with the literature on InAs/InAsSb superlattices detectors [13]. The L_{diff} of PD A is shorter than that of PD B, however, its effect on \mathfrak{R} is compensated by the larger α of PD A. A thicker $\text{Al}_{0.3}\text{InAsSb}$ absorber (up to ~ 3.5 μm) can increase \mathfrak{R} for PD B at 300 K, because its L_{diff} is approximately 3.5 μm at 300 K, as shown in Fig. 4(d). In addition, to increase the collection efficiency of holes at low temperature and thus D^* at $T = 120\text{--}180$ K, the $\text{Al}_{0.7}\text{InAsSb}$ barrier can be moved above the thick absorber. Shown in Fig. 1(b), the nBn structures operate with a lower bias applied to the barrier-side contact to facilitate hole transport to the barrier-side contact layer. With the barrier above the absorber where the incident photon flux is highest for the top-illuminated structure, more photogenerated holes can reach the contact at $T = 120\text{--}180$ K. Furthermore, high purity sources for MBE can also greatly help to further improve L_{diff} and thus Al_xInAsSb nBn device performance.

The smaller bandgap energy of $\text{Al}_{0.15}\text{InAsSb}$ enables PD A photodetection at 2.7 μm . The photoluminescence of the $\text{Al}_{0.15}\text{InAsSb}$ digital alloy peaks at ~ 3.0 μm at room temperature, which will be published elsewhere. The photodetection performance of PD A under 2.7- μm illumination was also measured to provide a comparison with that for 2- μm and a reference for 2.7- μm applications. Fig. 5 shows its room-temperature D^* and \mathfrak{R} for 2.7- μm illumination with current-voltage curves shown in the inset. The D^*_{peak} for 2.7- μm illumination is 4.9×10^9 Jones, which is lower than that for 2- μm illumination. This is primarily due to lower light absorption at 2.7 μm close to its cutoff. Based on the measured responsivity of PD A under 2.7- μm illumination and its C - V result at room temperature, its 2.7- μm absorption coefficient is derived to be 4533 cm^{-1} . Similarly, the absorption of $\text{Al}_{0.3}\text{InAsSb}$ decreases with wavelength in the spectral range from 1.7 to 2 μm ($E_{\text{photon}} \approx 0.73$ to 0.62 eV) which is close to its E_g of ~ 0.58 eV [9]. Such a wavelength dependence of absorption is well explained by the formula $\alpha \approx A^* \sqrt{E_{\text{photon}} - E_g}$, where A^* is a constant for a specified direct-bandgap semiconductor and E_{photon} is close to E_g .

V. CONCLUSION

This work demonstrates $\text{Al}_{0.15}\text{InAsSb}/\text{Al}_{0.7}\text{InAsSb}$ nBn photodetectors with high D^* at 2- μm and 2.7- μm wavelengths. An activation energy of ~ 0.42 eV, which is equal to the bandgap energy of the absorber, is derived from the Arrhenius plot for

$$\mathfrak{R} = \frac{q\lambda}{hc} (1-r) e^{-\alpha t} \left\{ \frac{\alpha L_{\text{diff}}}{\alpha^2 L_{\text{diff}}^2 - 1} \left[\frac{2\alpha L_{\text{diff}} - e^{-\alpha(H-w)} (e^b - e^{-b})}{e^b + e^{-b}} - \alpha L_{\text{diff}} e^{-\alpha(H-w)} \right] + e^{-\alpha(H-w)} (1 - e^{-\alpha w}) \right\} \quad (3)$$

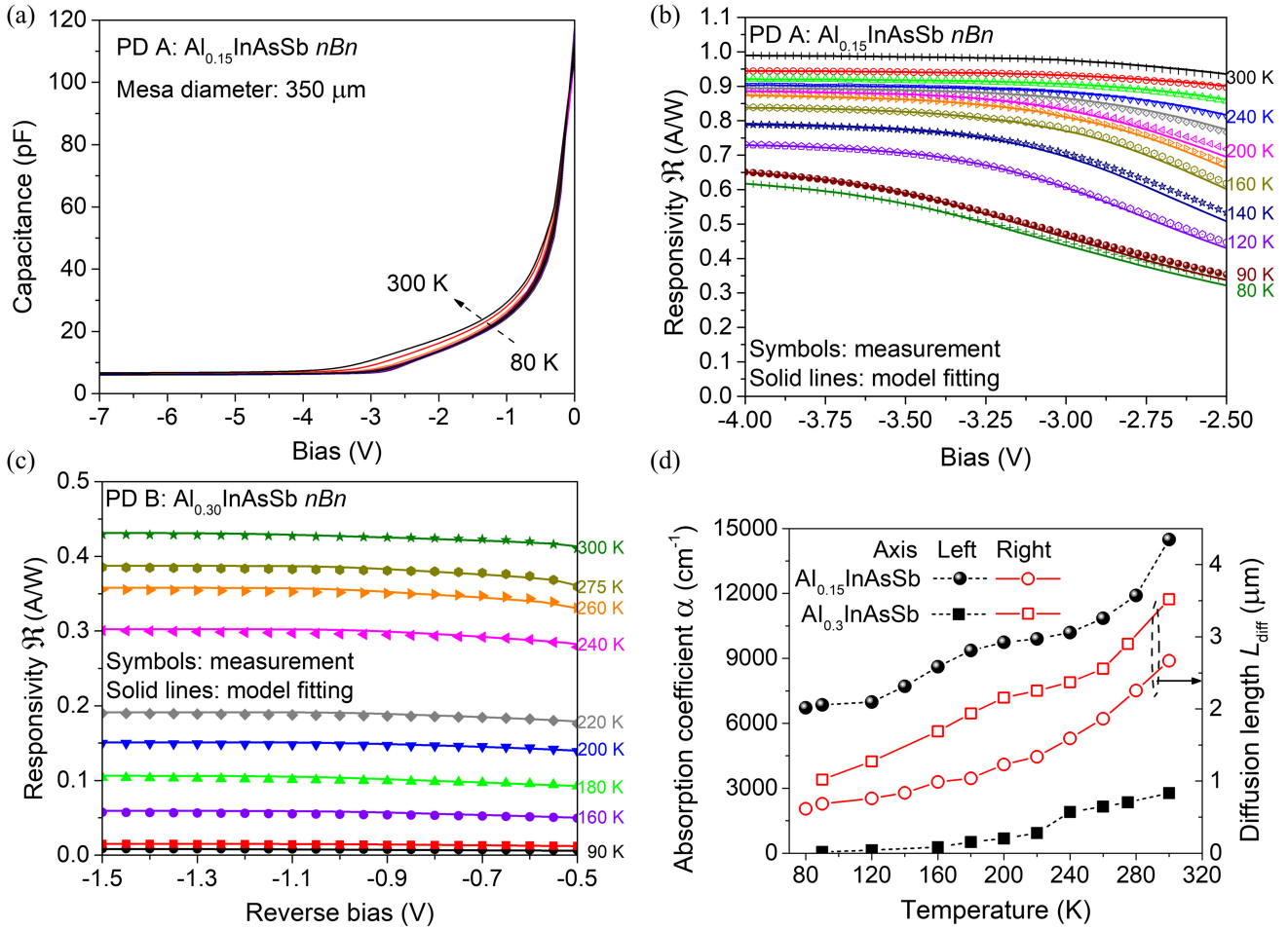


Fig. 4. (a) Measured C - V curves of a PD A at $T = 80$ -300 K. Measured and fitted responsivity versus applied bias for (b) PD A ($T = 80$ -300 K) and (c) PD B ($T = 90$ -300 K) under 2- μm illumination. (d) The derived 2- μm absorption coefficient (left axis) and minority carrier diffusion length (right axis) of PD A (circular symbols) and PD B (square symbols) at different temperatures. The diameter of the PD A and PD B device is 350 μm .

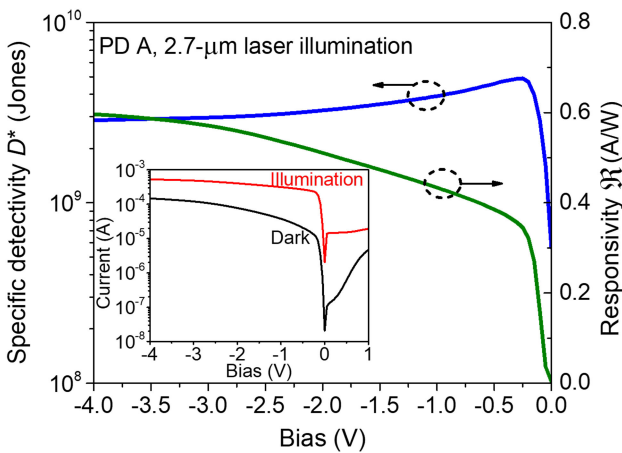


Fig. 5. D^* (left axis) and \mathfrak{R} (right axis) versus applied bias of a 350- μm -diameter PD A measured under 2.7- μm illumination at room temperature. The inset shows the current-voltage curves for dark and illumination conditions.

the diffusion-dominated regime. Close agreement was observed between J_d and D^* for the $\text{Al}_{0.15}\text{InAsSb}$ photodetectors with

different mesa diameters, whereas D^* of $\text{Al}_{0.3}\text{InAsSb } n\text{Bn}$ photodetectors decreases with decreasing diameter due to its surface-dominated J_d . With the decreasing temperature, the V_{peak} of the two photodetectors decreases to their minimum values in the diffusion/SRH-dominated regime, increase in the transitional region, and remain the same in the tunneling-dominated temperature range. With a lower doping concentration in the contact layer, V_{peak} can be significantly reduced without a compromise in the contact properties for the $\text{Al}_{0.15}\text{InAsSb}$ devices. At $T = 220$ -300 K, higher D^* was obtained from the $\text{Al}_{0.3}\text{InAsSb}$ photodetectors. With decreasing temperature, a larger D^* improvement was measured for the $\text{Al}_{0.15}\text{InAsSb}$ photodetectors than for $\text{Al}_{0.3}\text{InAsSb}$. At $T = 90$ -200 K, the higher D^*_{peak} in the range of 0.6 - 2.5×10^{12} Jones was achieved from the $\text{Al}_{0.15}\text{InAsSb}$ photodetectors. This is primarily due to a smaller temperature dependence of the $\text{Al}_{0.15}\text{InAsSb}$ absorption coefficient at 2 μm and a steep decrease in J_d and $1/RA$ with decreasing temperature at $T = 180$ -300 K. With the information of the measured V_{peak} , and the derived α and L_{diff} at different temperatures, this paper presents approaches and methods to further improve the figure-of-merit performance of $\text{Al}_x\text{InAsSb } n\text{Bn}$ photodetectors.

REFERENCES

- [1] A. P. Craig, A. R. J. Marshall, Z. B. Tian, S. Krishna, and A. Krier, "Mid-infrared InAs_{0.79}Sb_{0.21}-based *nBn* photodetectors with Al_{0.9}Ga_{0.2}As_{0.1}Sb_{0.9} barrier layers, and comparisons with InAs_{0.87}Sb_{0.13} p-i-n diodes, both grown on GaAs using interfacial misfit arrays," *Appl. Phys. Lett.*, vol. 103, no. 25, 2013, Art. no. 253502.
- [2] S. Maimon and G. W. Wicks, "*nBn* detector, an infrared detector with reduced dark current and higher operating temperature," *Appl. Phys. Lett.*, vol. 89, no. 15, 2006, Art. no. 151109.
- [3] E. Delli *et al.*, "Mid-infrared InAs/InAsSb superlattice *nBn* photodetector monolithically integrated onto silicon," *ACS Photon.*, vol. 6, no. 2, pp. 538–544, 2019.
- [4] D. Z. Ting *et al.*, "Long wavelength InAs/InAsSb superlattice barrier infrared detectors with p-type absorber quantum efficiency enhancement," *Appl. Phys. Lett.*, vol. 118, no. 13, 2021, Art. no. 133503.
- [5] A. Soibel *et al.*, "Mid-wavelength infrared InAsSb/InAs *nBn* detectors and FPAs with very low dark current density," *Appl. Phys. Lett.*, vol. 114, no. 16, 2019, Art. no. 161103.
- [6] J. B. Rodriguez *et al.*, "*nBn* structure based on InAs/GaSb type-II strained layer superlattices," *Appl. Phys. Lett.*, vol. 91, no. 4, 2007, Art. no. 043514.
- [7] N. Li *et al.*, "The investigations to eliminate the bias dependency of quantum efficiency of InGaAsSb *nBn* photodetectors for extended short wavelength infrared detection," *Infrared Phys. Technol.*, vol. 111, 2020, Art. no. 103461.
- [8] J. Zheng *et al.*, "Characterization of band offsets in Al_xIn_{1-x}As_ySb_{1-y} alloys with varying Al composition," *Appl. Phys. Lett.*, vol. 115, no. 12, 2019, Art. no. 122105.
- [9] D. Chen *et al.*, "Demonstration of infrared *nBn* photodetectors based on the AllnAsSb digital alloy materials system," *Appl. Phys. Lett.*, vol. 119, no. 3, 2021, Art. no. 031101.
- [10] R. Wang *et al.*, "Al_{0.3}InAsSb/Al_{0.7}InAsSb digital alloy *nBn* photodetectors," *J. Lightw. Technol.*, vol. 40, no. 1, pp. 113–120, Jan. 2022.
- [11] G. Bishop *et al.*, "*nBn* detectors based on InAs/GaSb type-II strain layer superlattice," *J. Vac. Sci. Technol. B: Microelectron. Nanometer Structures*, vol. 26, no. 3, 2008, Art. no. 1145.
- [12] E. Zielinski, H. Schweizer, K. Streubel, H. Eisele, and G. Weimann, "Excitonic transitions and exciton damping processes in InGaAs/InP," *J. Appl. Phys.*, vol. 59, no. 6, pp. 2196–2204, 1986.
- [13] A. Soibel, D. Z. Ting, A. M. Fisher, A. Khoshakhlagh, B. Pepper, and S. D. Gunapala, "Temperature dependence of diffusion length and mobility in mid-wavelength InAs/InAsSb superlattice infrared detectors," *Appl. Phys. Lett.*, vol. 117, no. 23, 2020, Art. no. 231103.
- [14] S. J. Maddox, S. D. March, and S. R. Bank, "Broadly tunable AllnAsSb digital alloys grown on GaSb," *Cryst. Growth Des.*, vol. 16, no. 7, pp. 3582–3586, 2016.
- [15] K. Scholle, S. Lamrini, P. Koopmann, and P. Fuhrberg, "2 μ m laser sources and their possible applications," in *Frontiers in Guided Wave Optics and Optoelectronics*. B. Pal, London, U.K.: IntechOpen, 2010, ch. doi: 10.5772/3033.
- [16] A. H. Jones, S. D. March, S. R. Bank, and J. C. Campbell, "Low-noise high-temperature AllnAsSb/GaSb avalanche photodiodes for 2- μ m applications," *Nature Photon.*, vol. 14, no. 9, pp. 559–563, 2020.
- [17] M. Hansen and D. Malchow, "Overview of SWIR detectors, cameras, and applications," in *Proc. SPIE Defense Secur. Symp.*, 2008, Art. no. 69390I.
- [18] R. W. M. Hoogeveen, R. J. van der A., and A. P. H. Goede, "Extended wavelength InGaAs infrared (1.0–2.4 μ m) detector arrays on SCIAMACHY for space-based spectrometry of the earth atmosphere," *Infrared Phys. Technol.*, vol. 42, no. 1, pp. 1–16, Feb. 2001.
- [19] W. Fu, J. Ma, P. Chen, and F. Chen, "Remote sensing satellites for digital Earth," in *Manual of Digital Earth*. H. Guo, M. F. Goodchild, and A. Annoni Eds., Singapore: Springer, 2020, pp. 55–123.
- [20] M. Jain *et al.*, *Development of an Ultrahigh-Performance Infrared Detector Platform For Advanced Spectroscopic Sensing Systems*. Bellingham, WA, USA: SPIE, 2014.
- [21] D. Hoffman, B.-M. Nguyen, P.-Y. Delaunay, A. Hood, M. Razeghi, and J. Pellegrino, "Beryllium compensation doping of InAs/GaSb infrared superlattice photodiodes," *Appl. Phys. Lett.*, vol. 91, no. 14, 2007, Art. no. 143507.
- [22] "Finite difference time domain (FDTD) solver," Accessed: Jan. 31, 2022, [Online]. Available: <https://support.lumerical.com/hc/en-us/articles/360034914633-Finite-Difference-Time-Domain-FDTD-solver-introduction>
- [23] "CHARGE solver introduction," Accessed: Jan. 31, 2022, [Online]. Available: <https://support.lumerical.com/hc/en-us/articles/360034917693-CHARGE-solver-introduction>
- [24] "Semiconductor material model properties," Accessed: Jan. 31, 2022, [Online]. Available: <https://support.lumerical.com/hc/en-us/articles/360034919113-Semiconductor-Material-Model-Properties>
- [25] A. H. Jones, "Al_xIn_{1-x}As_ySb_{1-y} digital alloy avalanche photodiodes for low-noise applications," Ph.D. dissertation, Dept. Elect. Eng., Univ. Virginia, Charlottesville, VA, USA, 2020.
- [26] S. Adachi, "Band gaps and refractive indices of AlGaAsSb, GaInAsSb, and InPAsSb: Key properties for a variety of the 2–4- μ m optoelectronic device applications," *J. Appl. Phys.*, vol. 61, no. 10, pp. 4869–4876, 1987.
- [27] S. M. Sze and K. K. Ng, *Physics of Semiconductor Devices*, 3rd. ed., Hoboken, NJ, USA: Wiley, 2007.
- [28] M. Ren, S. J. Maddox, M. E. Woodson, Y. Chen, S. R. Bank, and J. C. Campbell, "Characteristics of Al_xIn_{1-x}As_ySb_{1-y} (x:0.3–0.7) avalanche photodiodes," *J. Lightw. Technol.*, vol. 35, no. 12, pp. 2380–2384, Dec. 2017.
- [29] V. Gopal, E. Plis, J. B. Rodriguez, C. E. Jones, L. Faraone, and S. Krishna, "Modeling of electrical characteristics of midwave type II InAs/GaSb strain layer superlattice diodes," *J. Appl. Phys.*, vol. 104, no. 12, 2008, Art. no. 124506.
- [30] O. Gravrand *et al.*, "HgCdTe detectors for space and science imaging: General issues and latest achievements," *J. Electron. Mater.*, vol. 45, no. 9, pp. 4532–4541, 2016.
- [31] S. J. Maddox, W. Sun, Z. Lu, H. P. Nair, J. C. Campbell, and S. R. Bank, "Enhanced low-noise gain from InAs avalanche photodiodes with reduced dark current and background doping," *Appl. Phys. Lett.*, vol. 101, no. 15, 2012, Art. no. 151124.
- [32] N. Zhang, A. H. Jones, Z. Deng, and B. Chen, "Defect characterization of AllnAsSb digital alloy avalanche photodetectors with low frequency noise spectroscopy," *Opt. Exp.*, vol. 28, no. 8, pp. 11682–11691, Apr. 13, 2020.
- [33] T. Tredwell, "(Hg,Cd)Te photodiodes for detection of two-micrometer infrared radiation," *Opt. Eng.*, vol. 16, no. 3, 1977, Art. no. 163237.
- [34] H. Lotfi *et al.*, "Short-wavelength interband cascade infrared photodetectors operating above room temperature," *J. Appl. Phys.*, vol. 119, no. 2, 2016, Art. no. 023105.
- [35] S. Du *et al.*, "A broadband fluorographene photodetector," *Adv. Mater.*, vol. 29, no. 22, Jun. 2017, Art. no. 1700463.
- [36] Z. Djuric and Z. Jaksic, "Back side reflection influence on quantum efficiency of photovoltaic devices," *Electron. Lett.*, vol. 24, no. 17, pp. 11001101, 1988.
- [37] J. Klem, J. K. Kim, M. Cich, S. Hawkins, T. Fortune, and J. Rienstra, "Comparison of *nBn* and *nBp* mid-wave barrier infrared photodetectors," in *Proc. 7th SPIE OPTO, Quantum Sens. Nanophoton. Devices*, San Francisco, CA, USA, 2010, Art. no. 76081P. [Online]. Available: <https://doi.org/10.1117/12.842772>
- [38] I. Strzalkowski, S. Joshi, and C. R. Crowell, "Dielectric constant and its temperature dependence for GaAs, CdTe, and ZnSe," *Appl. Phys. Lett.*, vol. 28, no. 6, pp. 350–352, 1976.

Renjie Wang received the B.S. degree in energy engineering from Zhejiang University, Hangzhou, China, in 2010, the M.S. degree in mechanical engineering from the University of Houston, Houston, TX, USA, in 2012, and the Ph.D. degree in electrical engineering from McGill University, Montreal, QC, Canada, in 2018. He is currently a Research Associate with the Department of Electrical and Computer Engineering, University of Virginia, Charlottesville, VA, USA. His research interests include III-V optoelectronic device design, material growth, device fabrication, and device characterization.

J. Andrew McArthur received the B.S. degree in mechanical engineering from the University of Arkansas, Fayetteville, AR, USA. He is currently working toward the master's/Ph.D. degrees with the University of Texas, Austin, TX, USA. His primary research focuses on the design and epitaxial growth of III-V photodiodes in the near- and mid-infrared wavelength range.

Seth R. Bank (Fellow, IEEE) received the B.S. degree in electrical engineering from the University of Illinois at Urbana-Champaign (UIUC), Urbana, IL, USA, in 1999, and the M.S. and Ph.D. degrees in electrical engineering from Stanford University, Stanford, CA, USA, in 2003 and 2006, respectively. While with UIUC, he studied the fabrication of InGaP–GaAs and InGaAs–InP HBTs. His Ph.D. research interests include the MBE growth, fabrication, and device physics of long-wavelength VCSELs and low-threshold edge-emitting lasers in the GaInNAs(Sb)–GaAs material system. In 2006, he was a Postdoctoral Scholar with the University of California, Santa Barbara, CA, USA, where his research centered on the growth of metal–semiconductor hetero- and nano-structures, such as ErAs nanoparticles in GaAs. In 2007, he joined the University of Texas at Austin, Austin, TX, USA, where he is currently an Associate Professor of electrical and computer engineering and the holder of the fifth Temple Foundation Endowed Faculty Fellowship. He has coauthored more than 175 papers and presentations in his research field, which include the MBE growth of novel heterostructures and nanocomposites and their device applications. He was the recipient of the 2010 Young Investigator Program Award from ONR, 2010 NSF CAREER Award, 2009 Presidential Early Career Award for Scientists and Engineers (PECASE) nominated by ARO, 2009 Young Investigator Program Award from AFOSR, 2009 Young Scientist Award from International Symposium on Compound Semiconductors, 2008 DARPA Young Faculty Award, 2008 Young Investigator Award from the North American MBE Meeting, and several best paper awards.

Joe C. Campbell (Fellow, IEEE) received the B.S. degree in physics from the University of Texas at Austin, Austin, TX, USA, in 1969, and the M.S. and Ph.D. degrees in physics from the University of Illinois at Urbana-Champaign, Urbana, IL, USA, in 1971 and 1973, respectively. From 1974 to 1976, he was employed by Texas Instruments where he worked on integrated optics. In 1976, he joined the staff of AT&T Bell Laboratories in Holmdel, Holmdel, NJ, USA. In the Crawford Hill Laboratory, he was on a variety of optoelectronic devices including semiconductor lasers, optical modulators, waveguide switches, photonic integrated circuits, and photodetectors with emphasis on high-speed avalanche photodiodes for high-bit-rate lightwave systems. In January of 1989, he joined the Faculty of the University of Texas at Austin as a Professor of electrical and computer engineering and the Cockrell Family Regents Chair of engineering. In January of 2006, he became a Member of the Faculty with the University of Virginia, Charlottesville, VA, USA, as the Lucian Carr, III Chair of electrical engineering and applied science. To date, he has coauthored ten book chapters, 490 articles for refereed technical journals, and more than 450 conference presentations. His research interests include the optoelectronic components that are used to generate, modulate, and detect the optical signals. At present, he is actively involved in single-photon-counting avalanche photodiodes, Si-based optoelectronics, high-speed, low-noise avalanche photodiodes, ultraviolet photodetectors, and quantum-dot IR imaging. He is a Member of the National Academy of Engineering.